The Astrophysical Journal, 826:131 (11pp), 2016 August 1 doi:10.3847/0004-637X/826/2/131

SUPRATHERMAL ELECTRONS IN TITAN'S SUNLIT IONOSPHERE: MODEL–OBSERVATION COMPARISONS

E. Vigren[1], M. Galand[2], A. Wellbrock[3], A. J. Coates[3], J. Cui[4,5], N. J. T. Edberg[1], P. Lavvas[6], L. Sagnières[2], D. Snowden[7], V. Vuitton[8], and J.-E. Wahlund[1]
[1] Swedish Institute of Space Physics, Uppsala, Sweden; erik.vigren@irfu.se
[2] Department of Physics, Imperial College London, London SW7 2AZ, UK
[3] Mullard Space Science Laboratory, University College London, Dorking, Surrey RH5 6NT, UK
[4] National Astronomical Observatories, Chinese Academy of Sciences, Beijing 100012, China
[5] Lunar and Planetary Science Laboratory, Macau University of Science and Technology, Macau, China
[6] Université Reims Champagne-Ardenne, Reims, France
[7] Department of Physics, Central Washington University, Ellensburg, WA 98926, USA
[8] Univ. Grenoble Alpes, CNRS, IPAG, Grenoble, France
Received 2016 March 18; revised 2016 May 13; accepted 2016 May 20; published 2016 July 27

ABSTRACT

The dayside ionosphere of the Saturnian satellite Titan is generated mainly from photoionization of N_2 and CH_4. We compare model-derived suprathermal electron intensities with spectra measured by the *Cassini* Plasma Spectrometer/Electron Spectrometer (CAPS/ELS) in Titan's sunlit ionosphere (altitudes of 970–1250 km) focusing on the T40, T41, T42, and T48 Titan flybys by the *Cassini* spacecraft. The model accounts only for photoelectrons and associated secondary electrons, with a main input being the impinging solar EUV spectra as measured by the Thermosphere Ionosphere Mesosphere Energy and Dynamics/Solar EUV Experiment and extrapolated to Saturn. Associated electron-impact electron production rates have been derived from ambient number densities of N_2 and CH_4 (measured by the Ion Neutral Mass Spectrometer/Closed Source Neutral mode) and related energy-dependent electron-impact ionization cross sections. When integrating up to electron energies of 60 eV, covering the bulk of the photoelectrons, the model-based values exceed the observationally based values typically by factors of $\sim 3 \pm 1$. This finding is possibly related to current difficulties in accurately reproducing the observed electron number densities in Titan's dayside ionosphere. We compare the utilized dayside CAPS/ELS spectra with ones measured in Titan's nightside ionosphere during the T55–T59 flybys. The investigated nightside locations were associated with higher fluxes of high-energy (>100 eV) electrons than the dayside locations. As expected, for similar neutral number densities, electrons with energies <60 eV give a higher relative contribution to the total electron-impact ionization rates on the dayside (due to the contribution from photoelectrons) than on the nightside.

Key words: molecular processes – planets and satellites: individual (Titan)

1. INTRODUCTION

1.1. Briefly on Titan's Ionosphere and Its Ionization Balance

Titan, the largest satellite of Saturn, has an N_2- and CH_4-dominated atmosphere, the upper part of which has been probed by instruments on the *Cassini* spacecraft during 115 flybys, since the fall of 2004. The ionosphere, peaking typically at altitudes of 1000–1100 km, is composed of hydrocarbon ions, nitrile ions, and other complex organic molecular ions, including ones being negatively charged, and is now known to be an important source region for Titan's organic aerosols (e.g., Coates et al. 2007; Vuitton et al. 2007; Waite et al. 2007; Crary et al. 2009; Wahlund et al. 2009; Mandt et al. 2012; Lavvas et al. 2013; Wellbrock et al. 2013; Shebanits et al. 2013). The electron number density profile displays the basic variations anticipated from Chapman theory. In particular, on the dayside, the magnitude (altitude) of the ionospheric peak increases (decreases) with decreasing solar zenith angle (Ågren et al. 2009; Edberg et al. 2013), and the variations in the peak electron densities, over longer time periods, are also tightly linked to the incident solar EUV flux (Edberg et al. 2013).

There are, however, unresolved questions associated with the basics of Titan's ionosphere. For example, model calculations (Vuitton et al. 2009; Westlake et al. 2012) overestimate the number density of $HCNH^+$, the most abundant ion in Titan's ionosphere. Moreover, and probably related, while the shape of the electron number density profile in Titan's sunlit ionosphere is well understood and reproduced by solar-driven model calculations (impinging EUV spectra extrapolated from measurements by the Thermosphere Ionosphere Mesosphere Energy and Dynamics/Solar EUV Experiment, TIMED/SEE, Level 3; see Woods et al. 2005), the magnitude is off by a factor of ~2, with the models overestimating the Radio Plasma Wave Science/Langmuir probe (RPWS/LP) observations (Vigren et al. 2013). Whether the cause of the discrepancy is overestimated plasma production, underestimated plasma loss (e.g., due to missing loss processes), or a combination of both is an open question. Below we elaborate further on model–observation comparisons of electron number densities in Titan's ionosphere (Section 1.2). The calculated plasma production can be tested by different independent means, as described in Sections 1.3 and 1.4. The present study is primarily devoted to Titan's sunlit ionosphere and model–observation comparisons of suprathermal electron intensities. Earlier investigations of similar type are briefly summarized in Section 1.4.1, while Section 1.4.2 gives an overview of the present study.

1.2. Model–Observation Comparison of Electron Number Densities in the Sunlit and Nightside Ionosphere of Titan

The factor of ∼2 discrepancy between modeled and observed electron number densities in Titan's sunlit ionosphere (Vigren et al. 2013) is contrasted by a good level of agreement in the nightside ionosphere. Based on ambient suprathermal electron fluxes measured by the *Cassini* Plasma Spectrometer/Electron Spectrometer (CAPS/ELS) and N_2 and CH_4 number densities measured by the Ion Neutral Mass Spectrometer in the Closed Source Neutral mode (INMS/CNS), Vigren et al. (2015) calculated electron production rates at different locations along the T55–T59 Titan flybys by the *Cassini* spacecraft. The derived electron production rates were combined with estimates of the effective recombination coefficient, and the resulting plasma number densities (which were defined as the geometric mean of the electron and positive ion number densities) agreed well with values derived from RPWS/LP observations. The average ratio between modeled and observed plasma number densities for the nine investigated nightside locations was 1.05 with a standard deviation of 0.16 (for the dayside, when restricted to the T40 and T48 flybys, the mean ratio was 1.92 with a standard deviation of 0.08).

Introducing R as the ratio of the electron production and loss (through recombination), the above can be summarized in two equations roughly applicable at least in the altitude range 1050–1200 km on the dayside and 1100–1200 km on the nightside:

$$R_{\rm day} = \frac{P_{\rm e,day}}{n_{\rm pl}^2 \alpha_{\rm eff}} \approx 3.7 \pm 0.3 \quad (1a)$$

$$R_{\rm night} = \frac{P_{\rm e,night}}{n_{\rm pl}^2 \alpha_{\rm eff}} \approx 1.1 \pm 0.3, \quad (1b)$$

where $n_{\rm pl}$ denote plasma number densities derived from RPWS/LP measurements, $\alpha_{\rm eff}$ is the effective rate coefficient for dissociative recombination (number density weighted average of individual ion species' dissociative recombination rate coefficients; see Equation (4) in Vigren et al. 2013), and $P_{\rm e}$ is the electron production rate calculated from INMS/CSN-derived neutral number densities and impinging solar EUV spectra from TIMED/SEE (for the dayside) and suprathermal electron intensity spectra from CAPS/ELS (for the nightside). Only $P_{\rm e}$ is associated with a "day" or "night" index, as the other parameters were derived in similar manners. We note that $P_{\rm e,day}$ can be split up into two terms: $P_{\rm e,ph}$ (contribution from photoionization) and $P_{\rm e,EI}$ (contribution from impact ionization of photoelectrons, their secondaries, tertiaries, etc.). From model calculations the contribution of $P_{\rm e,EI}$ to the total dayside electron production rate is typically ∼20%–30% in the altitude range 1200–1000 km (see Figure 8 of Vigren et al. 2013). By equating the expressions for $R_{\rm day}$ and $R_{\rm night}$ and their current *average* values of ∼3.7 and ∼1.1, respectively, it is seen that in order for the average $R_{\rm day}$ and $R_{\rm night}$ to become roughly equal (not necessarily in the vicinity of 1, although that is ideal), an increase of $P_{\rm e,night}/P_{\rm e,day}$ by a factor of ∼3 is required. The $P_{\rm e}$ values depend partly on the neutral number density profiles. Based on the good agreement in shapes of modeled and observed electron number density profiles in the dayside ionosphere (Vigren et al. 2013), we will for the moment assume that the neutral number density profiles are not significantly off. Under this assumption, a derived dayside electron production rate, $P_{\rm e,day}$ (both the $P_{\rm e,ph}$ and $P_{\rm e,EI}$ terms), changes linearly with systematic changes across the utilized impinging solar EUV spectra (extrapolated from TIMED/SEE measurements). Likewise $P_{\rm e,night}$ changes linearly with systematic changes across the utilized suprathermal electron spectra (taken from measurements by CAPS/ELS).

1.3. Studies into Photoionization Rates in Titan's Ionosphere

Sagnières et al. (2015) compared N_2^+ and CH_4^+ production rates derived from their TIMED/SEE-based solar energy deposition model with production rates derived from an empirical chemical model driven by number densities of neutrals and (short-lived) ions measured by the INMS and laboratory-derived rate coefficients for key ion–neutral reactions. Below 1200 km the N_2^+ production rates derived from the solar energy deposition model agreed in shape but were a factor of $S_{\rm day} \sim 1.5$–2 higher than corresponding output values from the empirical chemical model (on the contrary, a good agreement was found between the model outputs of CH_4^+ production rates). For the nightside N_2^+ production rates derived from their CAPS/ELS-driven electron-impact ionization model were instead lower than production rates obtained from the empirical chemical model; $S_{\rm night} \sim 0.4$–0.7 (CH_4^+ production rates were not compared for the nightside ionosphere due to too low signal-to-noise ratios). If the discrepancy of N_2^+ production rates on any side (dayside or nightside) would be due to errors in the chemical reaction network (e.g., erroneous rate coefficients), then fixing the problem on the dayside would bring about even worse discrepancy on the nightside and vice versa. It follows, similar to the situation addressed in the previous paragraph, that in order for the dayside and nightside comparisons of N_2^+ production rates to become similar (i.e., for $S_{\rm day}$ and $S_{\rm night}$ to become similar), the solar EUV fluxes would need to be reduced (which would bring an issue on dayside CH_4^+ production rate comparisons) and/or the suprathermal electron fluxes would need to be somewhat enhanced with respect to the CAPS/ELS measurements across the energy bins contributing the greatest to the ionization of N_2. We note that Richard et al. (2015a) found better agreement between dayside N_2^+ production rates calculated from their solar energy deposition model and empirical chemical model than did Sagnières et al. (2015). This is most likely due to a combination of various factors: the calibration factor for INMS ion number densities (updated factor used by Sagnières et al.), different CH_4 and N_2 number densities, the correction factor in the empirical model from the inclusion of minor reactions, and a different solar flux model. These differences are discussed in depth in Section 4.6 of Sagnières et al. (2015).

1.4. Present Work: Suprathermal Electron Intensities in Titan's Ionosphere

In the present work we highlight discrepancies between model-derived (from our solar EUV energy deposition model) and observed (CAPS/ELS) suprathermal electron intensities in Titan's sunlit ionosphere. Similar model–observation comparisons have previously been performed by Robertson et al. (2009), Lavvas et al. (2011), and Richard et al. (2015a).

Table 1
Titan Flybys Considered in the Study with Information on Date, Saturn Local Time (SLT), and Taken at the Closest Approach (C/A), the Altitude of *Cassini*, the Solar Zenith Angle (SZA), Latitude, and Longitude

Flyby (Date)	SLT (hr)	C/A (km)	SZA (deg)	Latitude (deg)	Longitude (deg)
T40 (2008 Jan 5)	11.33	1014	38	12S	130
T41 (2008 Feb 22)	11.22	1000	30	35S	152
T42 (2008 Mar 25)	12.12	999	21	27S	157
T48 (2008 Dec 5)	10.37	961	25	10S	178

1.4.1. Earlier Investigations

In Robertson et al. (2009) model–observation comparisons of suprathermal electron fluxes were presented for the outbound of the T18 flyby at an altitude of 1210 km. For typical photoelectron energies (<60 eV) the modeled electron fluxes agreed quite well with CAPS/ELS observations, as can be seen in their Figure 4. Also Richard et al. (2015a), who presented comparisons for the outbound of the T40 flyby at 1020 km, obtained good agreement with CAPS/ELS observations (see their Figure 4), particularly over the electron energy range 10–60 eV. Among several potential sources of differences (not only directly model related; see Section 3.1), we merely note that Robertson et al. (2009) and Richard et al. (2015a) used solar flux models in their calculations (based on the solar $F_{10.7}$ value), while we in the present work, similar to that done by Lavvas et al. (2011), use solar EUV fluxes based on TIMED/SEE measurements. Regarding Lavvas et al. (2011), their modeled electron spectra acquired along the T40 flyby agreed reasonably in shape with CAPS/ELS observations for energies <60 eV. However, the modeled values were found elevated with respect to the observations, particularly so for altitudes of 1100 km and higher (see their Figure 7).

1.4.2. Overview and Outline of Present Study

In the present study we focus on a larger set of dayside flybys and make also quantitative comparisons of electron-impact electron production rates as calculated across different electron energy intervals. The solar-energy deposition model, based on Galand et al. (2010) and Vigren et al. (2013), is briefly described in Section 2. While Lavvas et al. (2011) focused only on the T40 flyby and utilized in their calculations a solar zenith angle fixed to 37°.5, we investigate here locations along the T40, T41, T42, and T48 flybys (see Table 1 for information) and use for each location the associated solar zenith angle. We use CAPS/ELS measurements primarily from anode 2 (see Section 2.2) rather than using the central anodes 4 and 5 or averaging over all anodes. We implement also updated neutral number density profiles of N_2 and CH_4 as deduced from INMS/CSN (Cui et al. 2012).

Similar to the case studied by Lavvas et al. (2011), we find (Section 3) that modeled electron intensities (and associated electron-impact ionization rates) exceed CAPS/ELS-derived values at energies below ~60 eV. The discrepancy is pronounced, typically by a factor of $\sim 3 \pm 1$. On the one hand, application of systematic adjustments of the utilized spectra, forcing the factor closer to ~1, would also bring the $R_{\rm day}$ and $R_{\rm night}$ values, as well as $S_{\rm day}$ and $S_{\rm night}$ values, closer to each other. On the other hand, the discrepancy is difficult to explain from estimated uncertainties in the involved measurements. The study, which also includes comparisons between CAPS/ELS dayside and nightside spectra for similar ambient neutral number densities (Section 3.2), is summarized in Section 4.

2. APPROACH APPLIED

2.1. Model

The derivation of electron fluxes is based on Galand et al. (2010) and only briefly described here. The first step in the multi-stream model is the generation of photoelectron spectra. The impinging solar EUV spectra (see Figure 5 of Vigren et al. 2013) are extrapolated in distance from daily-averaged observations by the TIMED/SEE (Level 3) (uncertainties discussed in Section 3.3). The attenuation of the EUV spectra is modeled through the Beer–Lambert law and is a function of the number density profiles of N_2 and CH_4 as derived from measurements by the INMS/CSN (see Cui et al. 2012; uncertainties discussed below), associated photoabsorption cross sections (Samson et al. 1987, 1989), and the local solar zenith angle. The photoelectron spectrum is retrieved by combining the attenuated solar EUV flux with ambient neutral number densities and partial photoionization cross sections with associated ionization potentials.

In a second step the suprathermal electron intensity spectrum is obtained by solving the Boltzmann equation assuming steady-state conditions (Rees 1989). The profiles of the photoelectron source function and the number densities of N_2 and CH_4 from INMS/CSN are used as input into the latter calculation, together with the cross sections and excitation/ionization energies for electron-impact processes on N_2 (Majeed & Strickland 1997; Shemansky & Liu 2005; Itikawa 2006) and CH_4 (Erwin & Kunc 2005, 2008; Liu & Shemansky 2006).

An alternative, more approximate approach to derive electron-impact ionization rates is through the Electron Energy Degradation (EED) model presented by Vigren et al. (2013), which uses the local approximation (validated below 1200 km as shown in Lavvas et al. 2011) and also adopts energy-dependent expectation values for the electron energy loss due to impact ionization and electronic excitation. The model is described in the appendix of Vigren et al. (2013). Very briefly photoelectrons are distributed onto a grid with energy bins of width 1 eV. Calculations associated with energy bin k dictate how electrons (energy degraded or newly produced from electron-impact ionization) are distributed to energy bins $<k$. The differential number flux (with units $\rm cm^{-2}\,s^{-1}\,sr^{-1}\,eV^{-1}$) in the energy bin k can be retrieved from the number of newly produced electrons (per s, $\rm cm^3$, and eV), the ambient N_2 and CH_4 number densities, and the associated energy-dependent

Table 2
Electron-impact Electron Production Rates (cm^{-3} s^{-1}) Calculated from Equation (1) from Model-derived and Observationally (CAPS/ELS) Derived Differential Number Fluxes

Location Information	$P_{e,EI}$ "Full Range"		$P_{e,EI}$ $12.6 < E < 30$ eV		$P_{e,EI}$ $30 < E < 60$ eV		$P_{e,EI}$ 60 eV $< E < 10$ keV	
	Model	ELS	Model	ELS	Model	ELS	Model	ELS
T40in;**1239**;56;2.4;*57*[a]	0.53	0.28	0.28	0.09	0.24	0.07	0.02	0.11
T40in;**1144**;254;5.4;*52*	2.03	0.97	0.99	0.32	0.95	0.27	0.09	0.38
T40in;**1074**;814;10.8;*48*	4.47	2.96	1.91	0.88	2.30	0.97	0.25	1.11
T40in;**1035**;1305;16.2;*43*	5.07	3.23	1.90	0.93	2.79	0.87	0.37	1.44
T40out;**1021**;1480;18.3;*34*	5.64	3.77	2.10	1.02	3.12	1.12	0.42	1.63
T40out;**1056**;928;12.3;*29*	5.13	3.40	2.20	0.95	2.64	1.05	0.29	1.40
T40out;**1121**;382;6.7;*25*	3.03	1.66	1.47	0.55	1.43	0.42	0.13	0.68
T40out;**1201**;88;3.0;*21*	0.83	0.46	0.43	0.14	0.37	0.11	0.03	0.21
T41in;**1191**;49;1.9;*47*	0.45	0.22	0.23	0.07	0.21	0.06	0.02	0.09
T41in;**1107**;223;5.4;*43*	1.83	0.79	0.90	0.27	0.86	0.17	0.07	0.34
T41in;**1054**;679;11.4;*39*	4.50	2.31	2.07	0.71	2.23	0.69	0.21	0.92
T41in;**1012**;1662;24.6;*34*	7.44	3.96	2.96	1.13	4.01	1.02	0.47	1.82
T41out;**1015**;1738;26.2;*26*	7.84	4.64	3.14	1.16	4.22	0.98	0.49	2.50
T41out;**1058**;745;12.4;*21*	5.18	2.16	2.41	0.77	2.54	0.60	0.24	0.79
T41out;**1129**;140;3.9;*18*	1.23	0.47	0.62	0.16	0.57	0.13	0.05	0.17
T41out;**1200**;37;1.7;*16*	0.35	0.16	0.18	0.06	0.16	0.04	0.01	0.05
T42in;**1234**;54;3.0;*40*	0.52	0.47	0.27	0.10	0.23	0.11	0.02	0.26
T42in;**1133**;220;7.9;*36*	1.84	1.33	0.91	0.37	0.85	0.31	0.07	0.64
T42in;**1066**;601;15.7;*32*	3.96	2.14	1.82	0.70	1.95	0.68	0.19	0.77
T42in;**1021**;1158;24.8;*27*	5.64	3.47	2.32	1.02	2.97	0.96	0.34	1.49
T42out;**1006**;1462;28.7;*19*	6.10	4.36	2.38	1.13	3.31	1.27	0.42	1.95
T42out;**1045**;868;19.7;*14*	5.13	2.67	2.27	0.97	2.59	0.77	0.27	0.93
T42out;**1109**;362;11.0;*12*	2.89	1.48	1.41	0.50	1.36	0.40	0.12	0.58
T42out;**1191**;95;4.1;*11*	0.89	0.36	0.46	0.14	0.40	0.11	0.03	0.11
T48in;**1134**;131;6.1;*19*	0.96	0.52	0.52	0.16	0.40	0.13	0.03	0.23
T48in;**1060**;523;13.2;*19*	3.09	1.79	1.58	0.63	1.39	0.45	0.13	0.70
T48in;**998**;1252;26.2;*21*	4.88	3.43	2.16	0.95	2.44	0.85	0.27	1.63
T48in;**967**;2033;39.6;*23*	5.34	5.43	2.04	1.16	2.90	1.52	0.40	2.75
T48out;**984**;1868;33.9;*29*	5.23	4.63	2.05	1.27	2.81	1.31	0.37	2.06
T48out;**1110**;223;8.5;*38*	1.48	0.85	0.79	0.27	0.64	0.24	0.06	0.34
T48out;**1207**;52;3.6;*42*	0.41	0.25	0.23	0.07	0.17	0.06	0.01	0.11
T48out;**1247**;30;2.6;*43*	0.25	0.18	0.14	0.05	0.10	0.05	0.01	0.08

Note. Values are given for the 32 locations investigated and for a series of electron energy intervals as specified ("full range" refers to 12.6 eV $< E <$ 10 keV). From estimated/quoted uncertainties in involved measurements the uncertainties in the tabulated values (for $E < 60$ eV) are estimated as ~20%–25% (this neglects systematic uncertainties in neutral number densities; sensitivity tested separately).
[a] T40in;**1239**;56;2.4;*57* should be read as T40 inbound, altitude = 1239 km, $n(N_2) = 56 \times 10^7$ cm^{-3}, $n(CH_4) = 2.4 \times 10^7$ cm^{-3}, solar zenith angle ≈ 57°. Similarly, T48out means T48 outbound. Altitudes are written in bold only to guide readers.

electron-impact ionization cross sections of the species (see Equation (2) below).

2.2. Cassini Suprathermal Electron Observations

The CAPS/ELS instrument (Linder et al. 1998, pp. 257–262; Young et al. 2004; Lewis et al. 2010) is a hemispherical top-hat electrostatic analyzer measuring electrons in the energy range 0.6–28,000 eV. Each spectrum utilized in the present study was averaged from four consecutive recordings (each with a duration of 2 s, sweeping 63 energy levels). The instrument is equipped with eight angular sectors (anodes) each covering 20° × 5°. Negative ions, when present, typically contaminate the measurements in the central anodes, 4–5. For this reason and others (see discussion in Vigren et al. 2015) we have in the present study utilized the measurements from anode 2 of the CAPS/ELS instrument. By instead using anode 6, we obtain similar (within 15%) results to those presented in Tables 2–3 (see Section 3). This speaks in favor of the assumption of isotropic electron fluxes. For proper comparisons with modeled spectra we have corrected (applying Liouville's theorem) the measured spectra for the negative spacecraft potential as derived from RPWS/LP (around −0.6 to −1 V for all locations).

Apart from counting statistics uncertainties in the CAPS/ELS anode 2 derived suprathermal electron intensities, there is also an uncertainty of ~10% for energies less than 3 keV and ~20% above 3 keV due to uncertainties in the geometric factor of the instrument (see Lewis et al. 2010). Moreover, we have not corrected for (1) uncertainties due to possible local spacecraft obscuration effects on anode 2 data and (2) RTG background (Arridge et al. 2009). The uncertainties due to these effects are expected to be small in comparison to the other dominant uncertainties described above.

2.3. Calculations of Electron-impact Electron Production Rates

The electron-impact electron production rates $P_{e,EI,X}$ (where X is M if from the model, or O if from CAPS/ELS spectra) associated with impacting electron energies between E_{low} and E_{high} are calculated from modeled or

Table 3
Ratios of Electron-impact Electron Production Rates Derived from Modeled and Observed Differential Number Fluxes, $P_{e,EI,M}/P_{e,EI,O}$

Location Information	"Full Range"	12.6 eV < E < 30 eV	30 eV < E < 60 eV	60 eV < E < 10 keV
T40in;**1239**;56;2.4;*57*[a]	1.93	3.02	3.34	0.17
T40in;**1144**;254;5.4;*52*	2.09	3.11	3.57	0.23
T40in;**1074**;814;10.8;*48*	1.51	2.17	2.37	0.23
T40in;**1035**;1305;16.2;*43*	1.57	2.06	3.22	0.26
T40out;**1021**;1480;18.3;*34*	1.50	2.07	2.79	0.26
T40out;**1056**;928;12.3;*29*	1.51	2.32	2.51	0.21
T40out;**1121**;382;6.7;*25*	1.83	2.65	3.42	0.19
T40out;**1201**;88;3.0;*21*	1.80	2.97	3.43	0.15
T41in;**1191**;49;1.9;*47*	2.04	3.24	3.66	0.18
T41in;**1107**;223;5.4;*43*	2.32	3.32	4.90	0.22
T41in;**1054**;679;11.4;*39*	1.95	2.92	3.25	0.23
T41in;**1012**;1662;24.6;*34*	1.88	2.63	3.93	0.26
T41out;**1015**;1738;26.2;*26*	1.69	2.71	4.29	0.20
T41out;**1058**;745;12.4;*21*	2.39	3.12	4.25	0.30
T41out;**1129**;140;3.9;*18*	2.64	3.87	4.21	0.27
T41out;**1200**;37;1.7;*16*	2.25	2.90	3.93	0.24
T42in;**1234**;54;3.0;*40*	1.11 (1.12)	2.61 (2.66)	2.06 (2.08)	0.07 (0.07)
T42in;**1133**;220;7.9;*36*	1.39 (1.45)	2.47 (2.62)	2.70 (2.79)	0.12 (0.12)
T42in;**1066**;601;15.7;*32*	1.85 (2.05)	2.62 (3.00)	2.88 (3.11)	0.25 (0.26)
T42in;**1021**;1158;24.8;*27*	1.62 (1.94)	2.28 (2.90)	3.08 (3.54)	0.23 (0.24)
T42out;**1006**;1462;28.7;*19*	1.40 (1.73)	2.10 (2.82)	2.60 (3.09)	0.21 (0.22)
T42out;**1045**;868;19.7;*14*	1.93 (2.20)	2.35 (2.79)	3.36 (3.71)	0.29 (0.30)
T42out;**1109**;362;11.0;*12*	1.95 (2.06)	2.82 (3.02)	3.36 (3.49)	0.21 (0.21)
T42out;**1191**;95;4.1;*11*	2.46 (2.50)	3.27 (3.33)	3.67 (3.71)	0.30 (0.30)
T48in;**1134**;131;6.1;*19*	1.86	3.29	3.08	0.15
T48in;**1060**;523;13.2;*19*	1.73	2.50	3.06	0.18
T48in;**998**;1252;26.2;*21*	1.42	2.27	2.86	0.17
T48in;**967**;2033;39.6;*23*	0.98	1.76	1.90	0.15
T48out;**984**;1868;33.9;*29*	1.13	1.62	2.14	0.18
T48out;**1110**;223;8.5;*38*	1.75	2.92	2.67	0.16
T48out;**1207**;52;3.6;*42*	1.64	3.15	2.67	0.12
T48out;**1247**;30;2.6;*43*	1.37	2.70	2.17	0.10

Note. From estimated/quoted uncertainties in involved measurements; the tabulated values (for E < 60 eV) are estimated uncertain by ~27%. Values within parentheses displayed for the T42 flyby are associated with the use of neutral number densities reduced by a multiplicative factor of 2.1/2.9.
[a] T40in;**1239**;56;2.4;*57* should be read as T40 inbound, altitude = 1239 km, $n(N_2) = 56 \times 10^7$ cm^{-3}, $n(CH_4) = 2.4 \times 10^7$ cm^{-3}, solar zenith angle ≈ 57°. Similarly, T48out means T48 outbound. Altitudes are written in bold only to guide readers.

observed differential number fluxes $I_{e,X}$ (where X is M or O) according to

$$P_{e,EI,M} = 4\pi \sum_j n_j \int_{E=E_{low}}^{E_{high}} \sigma_j^{ioni}(E) I_{e,M}(E) dE, \quad (2a)$$

$$P_{e,EI,O} = 4\pi \sum_j n_j \int_{E=E_{low}}^{E_{high}} \sigma_j^{ioni}(E) I_{e,O}(E) dE, \quad (2b)$$

where the sum goes over species $j = N_2$ and CH_4, n denotes number density, and $\sigma_j^{ioni}(E)$ is the energy-dependent electron-impact ionization cross section of species j at energy E. For each investigated location we derive $P_{e,EI,M}$ and $P_{e,EI,O}$ values from the ionization threshold of CH_4 (12.6 eV) to 10 keV (we call this the "full range" noticing that extending the upper limit to 28 keV has a negligible influence on the results), in the energy range 12.6 eV < E < 30 eV, in the energy range 30 eV < E < 60 eV, and in the energy range 60 eV < E < 10 keV. The reason for inspecting separately the regions 12.6 eV < E < 30 eV and 30 eV < E < 60 eV is explained in Section 3.1.

The error from counting statistics in the INMS-derived N_2 number densities is <1% (Cui et al. 2012). When deriving neutral number densities from INMS measurements, Cui et al. (2012) used a calibration factor of 2.9 (see also Koskinen et al. 2011). While using as default the correction factor 2.9, we present in Section 3 also $P_{e,EI,M}/P_{e,EI,O}$ ratios obtained from the use of a calibration factor of 2.1 (slightly reduced from the value of 2.2 suggested by Teolis et al. 2015). A decrease of the utilized number density profiles by a multiplicative factor of 2.1/2.9 changes CAPS/ELS-derived electron production rates, $P_{e,EI,O}$, by the same multiplicative factor. The model-derived production rates, $P_{e,EI,M}$, are changed in a less straightforward fashion as the reduced neutral number density profiles affect the attenuation of the impinging solar EUV flux, moving the peak of the ion–electron pair formation downward in the ionosphere.

3. RESULTS AND DISCUSSION

3.1. Comparisons of Modeled and Observed Electron Intensities

In Figure 1 we show, for the ingress of T40 at ~1074 km, a comparison between differential number fluxes from the multi-stream model and those from CAPS/ELS (anode 2) measurements. Included in the figure are also results from the EED model, the results of which agree remarkably well with the more detailed model. Discrepancies between the model results

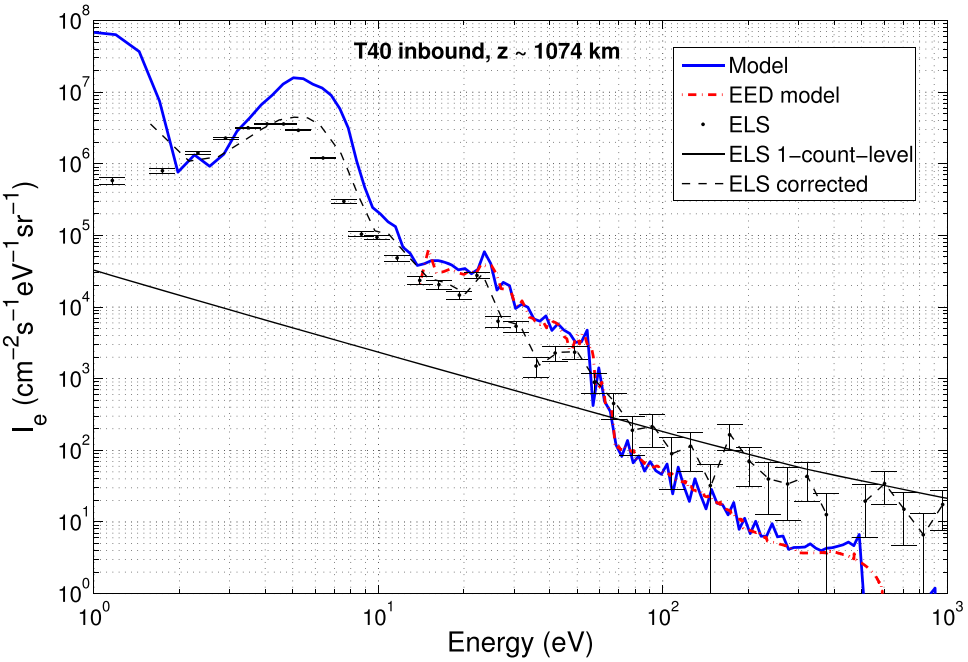

Figure 1. Comparison of model-derived differential number fluxes (blue line) with CAPS/ELS observations (black dots with associated error bars from counting statistics) for the ingress of the T40 flyby at an altitude near 1074 km. The red dot-dashed line shows results from the EED model, which only provides values at energies exceeding the lowest ionization potential of CH_4. The solid black line indicates the instrumental one-count level. The black dashed line shows the ELS fluxes corrected for a negative spacecraft potential of −1 V.

at energies exceeding 0.5 keV are mainly attributed to the use of different energy grids (the energy bin width is 1 eV in the EED model, while the energy grid in the multi-stream model is logarithmically spaced with bin widths spreading from 0.3 eV to 7 keV). The data in Figure 1 represent, for the investigated data set, a typical model–observation comparison of differential number fluxes.

It is seen in Figure 1 that for electron energies <60 eV, the modeled electron fluxes reasonably follow the variations in the observations, though being higher in magnitude by a factor of typically ∼2–2.5. This is reminiscent of the comparisons made by Lavvas et al. (2011) for the T40 flyby (see their Figure 7), who found modeled fluxes that were elevated with respect to CAPS/ELS observations for energies less than ∼60 eV particularly for altitudes near 1100 km and higher. The dip seen in the differential number flux between 2 and 5 eV is the result of vibrational excitation of N_2, whose associated electron-impact cross section peaks in this energy range (Galand et al. 2006; Lavvas et al. 2011). The model-predicted peak at ∼24 eV, corresponding to photoelectrons produced from the photoionization of N_2 by the strong solar He II line at 30.4 nm, is not as sharp (likely due to the energy resolution) but still present in the CAPS/ELS spectrum. The presence of this photoelectron peak signature has been noted in several earlier studies (e.g., Cravens et al. 2004; Galand et al. 2006, 2010; Lavvas et al. 2011; Wellbrock et al. 2012). The small shift in energy of the dominant peak is partly due to the spectral resolution but mainly due to the negative spacecraft potential. Correcting for the latter (dashed line in Figure 1) yields a better agreement in the position of the peak. For electron energies near ∼60 eV, the model predicts a sharp decrease in the electron flux (see Galand et al. 2006), which is not seen in the CAPS/ELS spectra. As such, for electron energies higher than ∼60 eV the situation reverses, with the modeled values being lower than the observed ones. This could, as discussed by Lavvas et al. (2011), be due to electrons of magnetospheric origin (not captured by the model) or relate to the fact that the fluxes toward higher energies correspond to count rates approaching the instrumental one-count level. We will in the following focus primarily on electron energies <60 eV.

In Table 2 we display for each considered location electron-impact electron production rates as calculated from Equation (2) using modeled and observed differential number fluxes across different energy intervals. In Table 3 we present the associated $P_{e,EI,M}/P_{e,EI,O}$ ratios. For wavelengths in the range 11–27 nm the TIMED/SEE output is based on scaling to measurements from the XUV Photometer System on the *SORCE* satellite (see Woods et al. 2005). Photoelectrons resulting from the ionization of N_2 into the ground state of N_2^+ are over this wavelength range associated with energies exceeding 30 eV. This motivates why we present in Table 2 $P_{e,EI,M}$ and $P_{e,EI,O}$ calculated separately for 12.6 eV $< E <$ 30 eV and for 30 eV $< E <$ 60 eV. We merely note from Table 3 that for 27 out of the 32 investigated locations the $P_{e,EI,M}/P_{e,EI,O}$ ratios for the 30 eV $< E <$ 60 eV interval are slightly higher than the ratios for the $E <$ 30 eV interval. Most notably, however, both intervals are associated with $P_{e,EI,M}/P_{e,EI,O}$ ratios typically in the range of 2–4. When considering the two intervals combined (i.e., 12.6 eV $< E <$ 60 eV), the set of 32 $P_{e,EI,M}/P_{e,EI,O}$ ratios has a mean value of 2.91 (standard deviation of the mean of 0.54).

As mentioned in Section 2.3, we apply as default an INMS/CSN calibration factor of 2.9. The influence on $P_{e,EI,M}/P_{e,EI,O}$ ratios of decreasing the neutral number densities by a multiplicative factor of 2.1/2.9 is exemplified from T42 data and revealed by values within parentheses in Table 3. At high altitudes (near 1200 km) the ratios remain similar (increases at most by a few percent), while deeper down (toward 1000 km) ratios are enhanced by up to ∼20% for the energy interval 30 eV $< E <$ 60 eV and by up to ∼35% for the energy interval

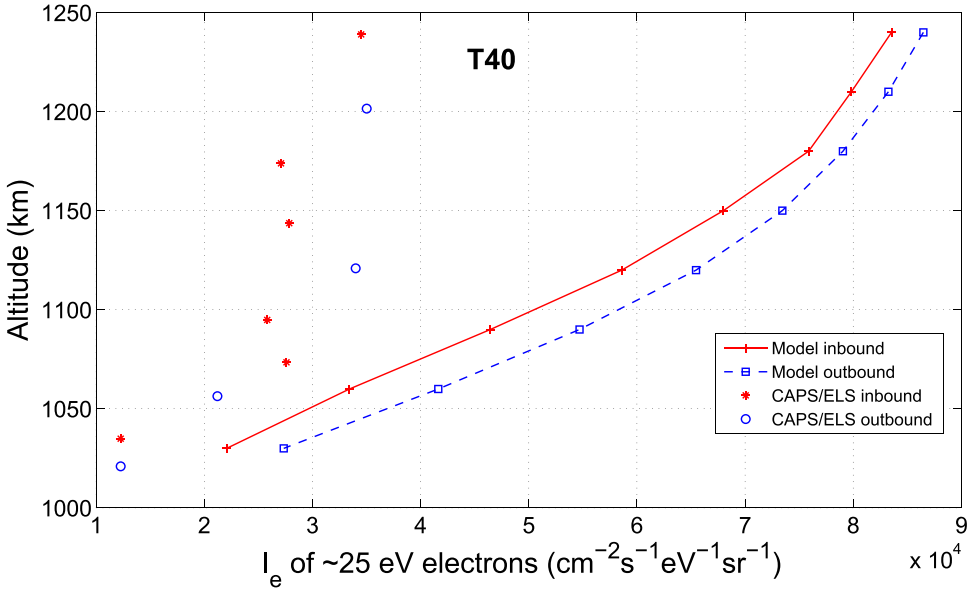

Figure 2. Shown vs. altitude along the T40 flyby are model-derived fluxes of electrons with energy ~25 eV. Shown also are CAPS/ELS (anode 2) measured fluxes of electrons from a nearby energy bin centered on 22.2 eV (not corrected for spacecraft potential). Statistical error margins (not shown) are on the level of 8%–14%.

12.6 eV $< E <$ 30 eV. The somewhat more pronounced influence in the 12.6 eV $< E <$ 30 eV energy interval is primarily associated with the wavelength dependence of the N_2 photoabsorption cross section.

It is interesting to inspect how the differential flux at a given electron energy changes with altitude. This is shown in Figure 2, where the modeled fluxes of ~25 eV electrons are plotted against altitude along the T40 flyby. Plotted also are CAPS/ELS-derived intensities from a nearby energy bin (central energy of 22.2 eV). The profile shape (going from high to low altitude)—decreasing more and more sharply—reflects to first approximation a decaying photoionization frequency due to atmospheric absorption. We observe roughly similar shapes in the observed and modeled profiles, with the modeled values being higher by a factor of ~2–2.5. The relative difference between modeled and observed values is somewhat higher at higher altitudes. This behavior could, similar to the tendency of $P_{e,EI,M}/P_{e,EI,O}$ ratios decaying with decreasing altitude, possibly be caused by the use of slightly (up to 20% or so) too high neutral number densities. It is stressed, however, that systematic errors in the utilized neutral number densities cannot explain the magnitude difference between modeled and observed electron fluxes. First, the utilized densities (or calibration factor) match those derived from measurements by the *Cassini* Ultraviolet Spectrograph (Koskinen et al. 2011), as well as those inferred from the *Cassini* Attitude and Articulation Control Subsystem and the Huygens Atmosphere Structure Instrument (Strobel 2010). Second, by systematically changing the utilized densities by ±50% removes the agreement with observed profile shapes, regarding both the model output of suprathermal electron fluxes and thermal electron number densities (see Vigren et al. 2013).

It was mentioned in Section 1.4.1 that the modeled electron fluxes by Robertson et al. (2009) and Richard et al. (2015a) were found to be in good agreement with CAPS/ELS observations. We plan to investigate in detail how the use of different solar EUV flux models affects the calculations of suprathermal electron intensities. In particular, it is of interest to find out whether discrepancies between such solar EUV flux models and spectra from TIMED/SEE are a contributing cause as to why our model predicts electron fluxes typically a factor of 2–4 higher than observed by CAPS/ELS (for electron energies <60 eV) while the model results of Robertson et al. (2009) and Richard et al. (2015a) show good agreement with observations. The different levels of agreement have several other potential/known causes as well. The use of somewhat different cross section sets and INMS neutral number density calibration factors may cause non-negligible differences in model output, particularly toward low altitudes. The model–observation comparison presented in Robertson et al. (2009) was for a rather high altitude of 1210 km during the outbound of the T18 flyby, a flyby not investigated in the present study. The solar zenith angle was ~80°.5 and so markedly higher than the range of solar zenith angles encountered in the present study (only high-altitude points along the inbound of T40 were associated with solar zenith angles >50°). In Richard et al. (2015a) the only presented model–observation comparison of electron fluxes was associated with the egress of T40 at ~1020 km. The good agreement between modeled and observed electron fluxes, particularly for electron energies 10 eV $< E <$ 25 eV, is reminiscent of what is shown in Figure 8 of Lavvas et al. (2011). It is noted that the CAPS/ELS averaged fluxes associated with the outbound of T40 at ~1020 km, as displayed in Figure 4 of Richard et al. (2015a) and Figure 8 of Lavvas et al. (2011), are higher in the energy range ~10–25 eV compared with the anode 2 based fluxes used in the present study for roughly the same location. The fluxes inferred from anode 2 measurements and used in the present study for T40 outbound at ~1021 km are ~3.0, 1.5, 1.7, 0.8, and 1.2 × 10^4 cm^{-2} s^{-1} eV^{-1} sr^{-1} for the energy bins centered on ~11.6, 14.0, 16.3, 19.3, and 22.2 eV, respectively. The associated fluxes inferred from anode 4 (anode 5) measurements are higher by 38%, 99%, 44%, 119%, and 28%, respectively (62%, 61%, 28%, 58%, and 32%, respectively). Such pronounced discrepancies between fluxes inferred from the central anodes and anode 2 are not seen at higher altitudes. Among the other locations (altitudes of 1056, 1121, and

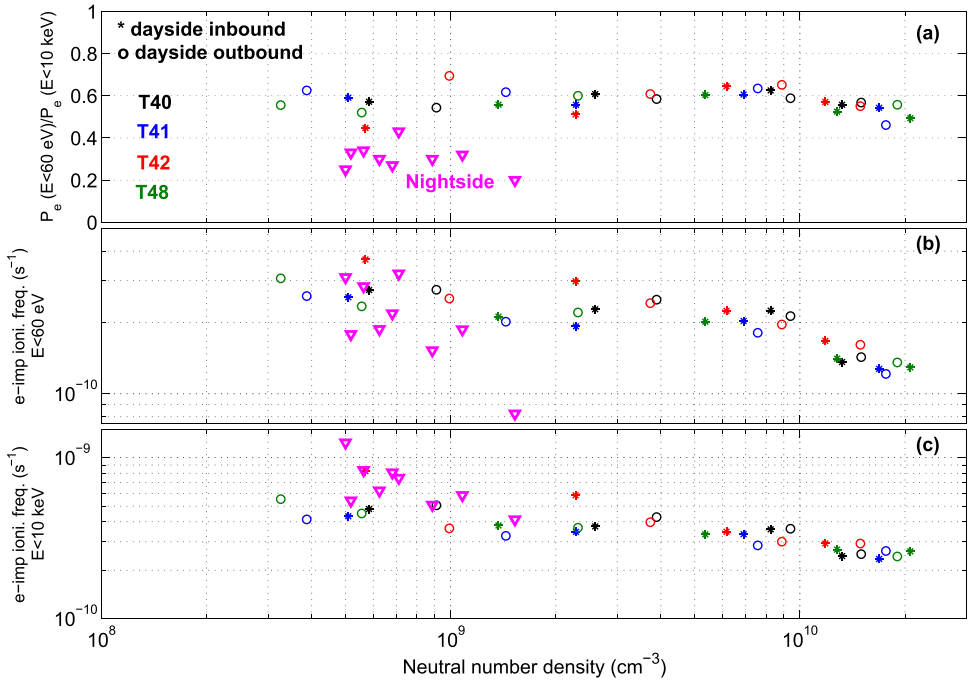

Figure 3. Shown as a function of ambient $N_2 + CH_4$ number densities (derived from INMS/CSN measurements) are (a) the relative contribution of <60 eV electrons to the CAPS/ELS-derived electron-impact ionization frequencies (electron energies up to 10 keV considered), (b) electron-impact ionization frequencies when limited to electrons with energies <60 eV, and (c) electron-impact ionization frequencies when limited to electrons with energies <10 keV. The nightside points (shown by magenta triangles) are taken from the study by Vigren et al. (2015) and are associated with the T55–T59 flybys.

1201 km) investigated along the egress of the T40 flyby, the fluxes measured in the same set of energy bins by the central anodes are in no case more than 20% elevated above the fluxes measured by anode 2.

3.2. CAPS/ELS-derived Electron-impact Ionization Frequencies on the Dayside and Nightside

In this subsection we focus explicitly on CAPS/ELS-derived electron production rates ($P_{e,EI,O}$) and view the present dayside results against results associated with the nine nightside locations (sampled from the T55–T59 flybys) investigated in the study by Vigren et al. (2015). In Figure 3(a) we display the contribution to the total electron-impact electron production rate of electrons with energies <60 eV. For comparable neutral number densities, n_N (=$n(N_2)$ + $n(CH_4)$), the nightside values are lower than the dayside values, which can be understood from the lack of a solar EUV input on the nightside, which on the dayside contributes with electrons primarily with energies <60 eV.

Effective electron-impact ionization frequencies are obtained by dividing electron-impact electron production rates by the ambient total neutral number density, n_N. In Figure 3(b) we show against n_N such ionization frequencies when limited to impacting electrons with energies <60 eV. We note that the nightside point associated with the highest n_N is markedly lower than dayside values of similar neutral number density. However, the mean of the seven nightside points with $n_N < 10^9\,cm^{-3}$ is equal to $(2.4 \pm 0.7) \times 10^{-10}\,s^{-1}$, only slightly lower than $(2.8 \pm 0.4) \times 10^{-10}\,s^{-1}$, the mean of the eight (less spread) dayside points associated with $n_N < 10^9\,cm^{-3}$. The electron-impact ionization frequencies derived from the full CAPS/ELS energy range are shown in Figure 3(c). In this case the nightside point with the highest n_N has an ionization frequency comparable with dayside values at similar n_N. The mean of the seven nightside points with $n_N < 10^9\,cm^{-3}$ is $(7.6 \pm 2.5) \times 10^{-10}\,s^{-1}$ and so higher than $(5.0 \pm 1.2) \times 10^{-10}\,s^{-1}$, the mean of the eight (less spread) dayside points associated with $n_N < 10^9\,cm^{-3}$.

The comparable dayside and nightside electron-impact ionization frequencies are interesting in light of the fact that the solar EUV input is lacking on the nightside. This indicates extensive differences in the flux levels of high-energy electrons of magnetospheric origin. Such differences are seen in Figure 4, which displays CAPS/ELS (anode 2) spectra for two dayside and two nightside locations, each associated with neutral number densities within the range $(9–11) \times 10^8\,cm^{-3}$. In this example, the nightside locations are clearly associated with higher fluxes of high-energy electrons ($E > 100$ eV) than the dayside locations.

Upstream electron fluxes at Titan can indeed vary substantially (see in particular Rymer et al. 2009; Arridge et al. 2011), and the electron precipitation also depends strongly on the magnetic field topology (Gronoff et al. 2009; Simon et al. 2013; Snowden et al. 2013; Edberg et al. 2015; Richard et al. 2015b). Clearly, from the limited set of flybys and locations investigated here we *cannot* state that magnetospheric electrons preferably are directed toward Titan's nightside. It is noted that the herein investigated sets of dayside and nightside flybys were associated with different Saturn Local Times (SLTs) and magnetospheric conditions (see Simon et al. 2013). The dayside flybys (T40, T41, T42, and T48) were all associated with SLTs in the narrow range of ~10–12 hr (see Table 1) but occurred in different magnetic environments according to the classification scheme of Simon et al. (2010, 2013). On the contrary, all of the considered nightside flybys (T55–T59) were associated with an SLT of ~22 hr and occurred within Saturn's oscillating current sheet (Simon et al. 2010, 2013).

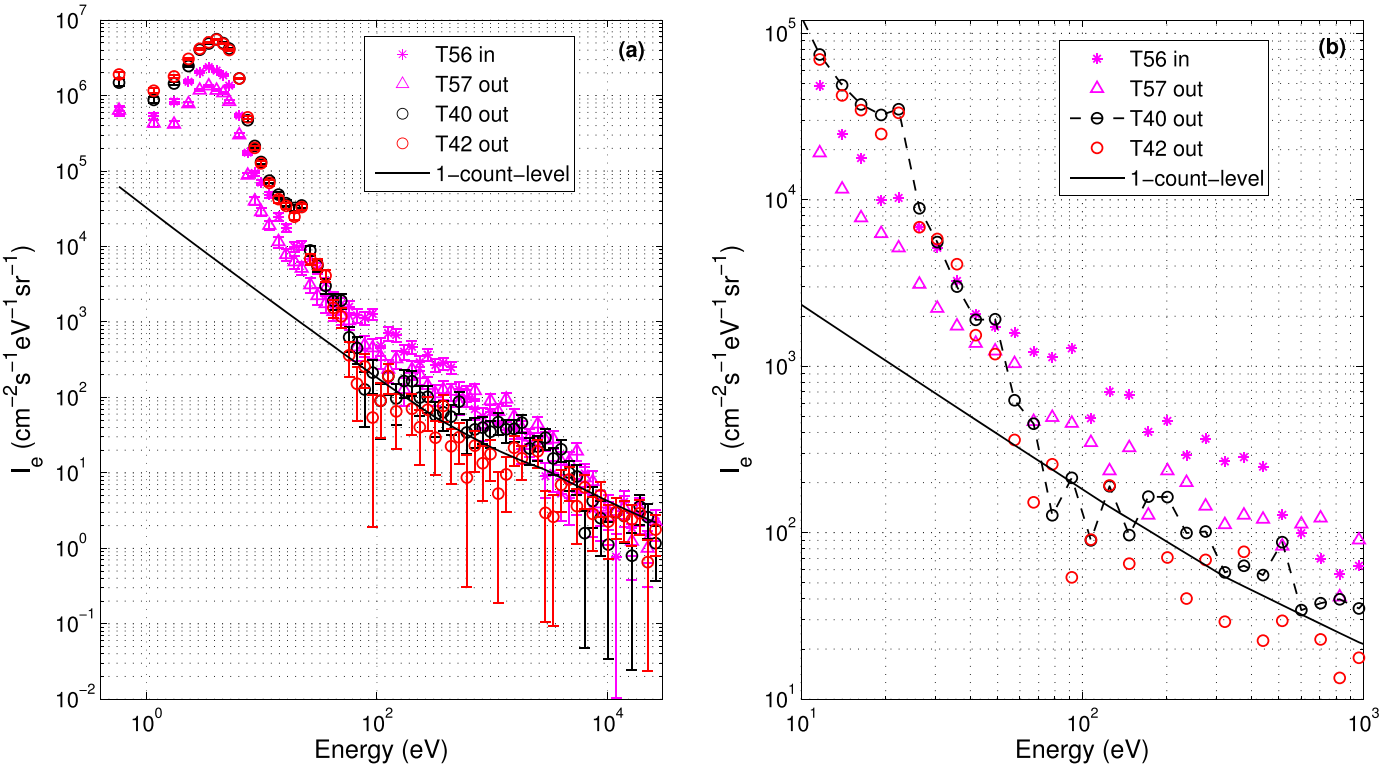

Figure 4. (a) Differential number fluxes observed by CAPS/ELS (anode 2) at locations during the nightside T56 and T57 flybys (magenta asterisks and triangles, respectively) and during the dayside T40 and T42 flybys (black and red circles, respectively). Each of the four locations was associated with an ambient neutral number density within the range (9–11) $\times$ 10^8 cm^{-3}. Errors from counting statistics are shown, and the black solid line is the instrumental one-count level. (b) Same data set, but over the energy range 10 eV to 1 keV and without error bars being showed.

In order to look for dependencies of, e.g., the solar zenith angle, the SLT, and the magnetic environment on the fluxes of high-energy electrons in Titan's upper atmosphere (at locations with similar neutral number densities), we are planning to conduct a study making use of CAPS/ELS and INMS/CSN data from an extended set of Titan flybys. It is noted that Edberg et al. (2015) performed a somewhat similar study, but with the focus on electron number densities measured by RPWS/LP. Using data from 109 Titan flybys and correcting for solar zenith angle and solar EUV variations, they reported that electron number densities in the altitude range 1600–2400 km are elevated by a factor of ~2.5 when Titan is located on Saturn's nightside compared with when located on the dayside. They also reported that variations in electron number densities in the altitude range 1100–1600 km are largely driven by magnetospheric conditions, with densities being enhanced typically by ~40% when Titan is located in the magnetospheric current sheet compared to when it is located in the magnetospheric lobes. The latter increase was proposed to reflect enhanced electron-impact ionization of ~200 eV sheet electrons.

3.3. Regarding Uncertainties in Measurements

The following error estimates are particularly for electron energies <60 eV and do not account for systematic errors in neutral number densities (discussed and sensitivity tested separately in Section 3.1; see Table 3). Using estimated/quoted uncertainties of involved input parameters, we arrive at error estimates of ~20%–25% for the $P_{e,EI,M}$ and $P_{e,EI,O}$ values listed in the subcolumns of columns (3) and (4) of Table 2. For the $P_{e,EI,O}$ values calculated from Equation (2), we used in the error propagation systematic uncertainties in anode 2 derived $I_{e,O}$ of 15% (the statistical uncertainties at energies <60 eV are small), an additional 15% uncertainty based on inter-anode variations in derived $I_{e,O}$ (variations between anode 2 and anode 6 measurements considered primarily), and a 10% uncertainty in the electron-impact ionization cross section. This gives a total uncertainty of ~23%. For $P_{e,EI,M}$ values we note first of all that the utilized cross sections for some of the electron-impact electronic excitation processes of N_2 are uncertain by as much as 40% (see Itikawa 2006). However, even when changing the cross sections of all the electron-impact electronic excitation channels (for both N_2 and CH_4) by ±40%, the calculated $P_{e,EI,M}$ values change by less than 7% (increased cross sections yielding decreased $P_{e,EI,M}$ values). We have also tested how computed $P_{e,EI,M}$ values are affected by changing (in different combinations) the utilized cross sections for photoionization, electron-impact electronic excitation, and electron-impact ionization by ±10% and the utilized impinging solar EUV fluxes by ±15%. While high-altitude points can increase by up to 35% (decrease by up to 30%) and low-altitude points by up to 30% (decrease by up to 25%), this happens only if all involved parameters are changed in specific directions. As a consequence, and after inspecting outputs from models where the involved parameters have been changed in different directions (or in part not changed at all), we consider uncertainty estimates of 20%–25% in the tabulated $P_{e,EI,M}$ values more appropriate. Noticing that systematic uncertainties in the electron-impact ionization cross sections affect $P_{e,EI,O}$ and $P_{e,EI,M}$ in the same way, the error estimate of ~27% in the $P_{e,EI,M}/P_{e,EI,O}$ ratios in Table 3 is slightly reduced from the value that would emerge if treating the estimated errors in

$P_{e,EI,O}$ and $P_{e,EI,M}$ as completely independent. Clearly, this estimated error is too low to explain $P_{e,EI,M}/P_{e,EI,O}$ ratios of $\sim 3 \pm 1$.

Significant unforeseen systematic errors in the TIMED/SEE data, stated accurate to within 5%–20% (Woods et al. 2008; Lean et al. 2011), are to be considered unlikely. The *Solar Dynamics Observatory* (*SDO*) was not yet operational during the investigated flybys, but it was for T83 and T86 (Woods et al. 2012). Sagnières et al. (2015) reported that for the latter flybys, the N_2^+ (and CH_4^+) production rates calculated along the *Cassini* trajectories were found to differ by less than 10% when using the solar flux from the *SDO*/EUV Variability Experiment instrument compared with TIMED/SEE. The extrapolation in distance of the solar EUV flux (measured) near Earth to Titan neglects EUV extinction (expected negligible) and does not correct for the phase difference between the objects. However, among the four flybys, only T48 occurred while the Earth–Sun–Saturn angle exceeded 45° (the angle was ∼130° for that flyby), and more importantly, for a fixed optically thin location and during a full solar rotation period (∼27 days) the *peak-to-dip* ratio of daily-averaged photoionization frequencies is typically only in the vicinity of 30%.

It should be noted that the geometric factor (for converting counts s^{-1} into fluxes) of CAPS/ELS was reduced by a multiplicative factor of 0.32 (from on-ground to in-flight values) following comparisons of electron number densities derived (during 2005 July 14, 10:00–11:00 UT) from CAPS/ELS observations and RPWS measurements of the upper hybrid frequency (Lewis et al. 2010). As the updated geometric correction factor was already implemented in the present study, a further reduction of the geometric correction factor by a factor of ∼3 would be required to force $P_{e,EI,O}$ values as calculated for $12.6\,\mathrm{eV} < E < 60\,\mathrm{eV}$ into an on-average good agreement with the associated $P_{e,EI,M}$ values. Identifying further appropriate times (and ideally closer in time to the flybys investigated here) for comparisons between CAPS/ELS- and RPWS-derived electron number densities would serve useful to further validate the in-flight geometric correction factor currently used. We note, however, that Lewis et al. (2010) did make additional comparisons (with data from other instruments and simulations) in order to verify the updated value and argued that the ELS is well calibrated and that the data can be used with confidence.

We note finally that by systematically enhancing the CAPS/ELS-derived fluxes by a factor of 3 (4) at electron energies <60 eV only is sufficient to reduce the average R_{day}/R_{night} ratio (see Section 1), currently at ∼3.4, to ∼2.1 (∼1.75). The reduction is not more pronounced since, as seen in Figure 2(a), the contribution of <60 eV electrons to the total electron-impact ionization rate is only on the level of 20%–40% (mean of 30.4% and a standard deviation of the mean of 6.5%) for the set of nightside points investigated. A systematic flux enhancement by a factor of 3.4 *across the full energy range* of CAPS/ELS would set $R_{day}/R_{night} \sim 1$. In this speculative scenario we get $R_{day} \approx R_{night} \approx 3.7$, and in order to reach the ideal R-values of 1 (provided validity of the assumption of photochemical equilibrium), furthermore an enhancement of $n_{pl}{}^2\alpha_{eff}$ by a factor of 3.7 is required. Such an increase conflicts with error estimates of the RPWS/LP-derived plasma number densities (∼10%) and the utilized effective recombination coefficients (see, e.g., Section 5.4 of Vigren et al. 2013).

4. SUMMARY AND CONCLUDING REMARKS

From reportedly well-constrained input parameters we have derived differential number fluxes of suprathermal electrons in Titan's main sunlit ionosphere. The model itself is of standard type, is applied to a region where the local approximation is expected valid (attested by the good agreement between the full model and the simpler EED model; see also Lavvas et al. 2011), and makes use of a well-constrained cross-section set (regarding electron-impact processes at least for $E < 1\,\mathrm{keV}$). The modeled fluxes have been compared with CAPS/ELS observations (see Figure 1). In addition, the modeled and observed fluxes have been used to generate electron-impact electron production rates, $P_{e,EI,M}$ and $P_{e,EI,O}$, respectively (see Equation (2) and Tables 2, 3).

The key findings of the study are summarized as follows.

1. Over the energy range $12.6\,\mathrm{eV} < E < 60\,\mathrm{eV}$, constituting the bulk of the photoelectron energy distribution, the modeled suprathermal electron intensities agree reasonably in shape with the CAPS/ELS observations. A peak around 24 eV, due to photoelectrons emerging from the photoionization of N_2 into N_2^+, appears in both the modeled and the observed spectra, as found also in previous studies (e.g., Galand et al. 2006; Lavvas et al. 2011).
2. However, modeled electron fluxes are typically higher than observed for $E < 60\,\mathrm{eV}$, with associated $P_{e,EI,M}/P_{e,EI,O}$ ratios typically around 3 ± 1 (see Table 3). The discrepancy is difficult to explain in view of estimated and quoted uncertainties in involved measurements.
3. At energies >60 eV, the modeled fluxes are lower than observed (sometimes by nearly an order of magnitude). This could be caused by the fact that the model only accounts for photoelectrons and their secondaries, tertiaries, etc., and so does not include contributions from magnetospheric electrons.

We have discussed the results in relation to other Titan ionospheric studies wherein ionization rates on the dayside are calculated from the TIMED/SEE-based solar EUV energy deposition model while ionization rates on the nightside are calculated from ambient neutral number densities and CAPS/ELS spectra of suprathermal electron intensities. We summarize the present understanding and findings as follows.

1. At present the modeled plasma number densities on the dayside are higher than the RPWS/LP-derived values by a factor of $\sim 1.92 \pm 0.08$. On the nightside the level of agreement is better, the modeled values being on average a factor of $\sim 1.05 \pm 0.16$ higher than observed (Vigren et al. 2013, 2015).
2. Modeled N_2^+ production rates on the dayside are higher (by a factor of ∼1.5–2) than derived from an empirical chemical model. On the nightside the situation is reversed, with the modeled production rates being lower than values from the empirical chemical model by a multiplicative factor of ∼0.4–0.7 (Sagnières et al. 2015).
3. Systematic adjustments of TIMED/SEE and/or CAPS/ELS spectra, forcing $P_{e,M}/P_{e,O}$ ratios for $E < 60\,\mathrm{eV}$ to values closer to ∼1, would affect the above-mentioned results. It would make the level of agreement with observations (with the empirical model in the case of N_2^+

production rates) more similar for the dayside and nightside ionospheres.

We have also compared the CAPS/ELS dayside spectra utilized in the present study against those used in the nightside study by Vigren et al. (2015). For comparable ambient neutral number densities, n_N (here limited to a few locations with $5 < n_N < 15 \times 10^8\,\mathrm{cm}^{-3}$), the nightside locations are associated with markedly higher fluxes of high-energy electrons (see Figure 4) than the dayside locations. We emphasized in Section 3.2 that the dayside flybys (T40–T42 and T48) occurred in different magnetic environments and SLTs of 10–12 hr, while all of the nightside flybys (T55–T59) occurred within Saturn's oscillating current sheet (see Simon et al. 2013) and at SLTs of ~22 hr. It is known from earlier studies that varying upstream conditions and the magnetic topology cause highly varying levels of electron fluxes in Titan's ionosphere (e.g., Gronoff et al. 2009; Rymer et al. 2009; Arridge et al. 2011; Snowden et al. 2013; Richard et al. 2015b). The present work, limited to a small set of flybys and locations, shows that the magnetospheric input alone at times can be so high that resulting electron-impact ionization frequencies (see Figure 3, panels (b) and (c)) become comparable to, or even higher than, electron-impact ionization frequencies in locations with similar n_N but subjected to solar EUV input and associated photoelectron generation.

As concluding words, the main motivation of this study was to investigate further whether overestimated plasma production is a contributing reason as to why models predict nearly a factor of 2 higher electron number densities than observed in Titan's sunlit and main ionosphere. While the finding that the modeled electron fluxes at typical photoelectron energies are markedly higher than measured by the CAPS/ELS (anode 2) is indicative of such an overestimation in plasma production, we wish to keep several possibilities open and therefore refrain from drawing (possibly too) strong conclusions.

E.V. is grateful for funding from the Swedish National Space Board (DNR 14/166). M.G. is partially funded by the Science & Technology Facilities Council (STFC) of UK under grant ST/K001051/1. N.J.T.E. acknowledges support from the Swedish Research Council and the Swedish National Space Board. A.J.C. and A.W. are thankful for support from STFC via the UCL-MSSL consolidated grant (ST/K000977/1). J.C. acknowledges support from the National Science Foundation of China (NSFC) through grants 41525015 and 41374178. Support for this work was provided by a Centre National d'Etudes Spatiales *Cassini* Participating Scientist grant (to V. V.). We thank an anonymous referee for valuable comments.

REFERENCES

Ågren, K., Wahlund, J.-E., Garnier, P., et al. 2009, P&SS, 57, 1821
Arridge, C. S., André, N., Bertucci, C. L., et al. 2011, SSRv, 162, 25
Arridge, C. S., Gilbert, L. K., Lewis, G. R., et al. 2009, P&SS, 57, 854
Coates, A. J., Crary, F. J., Lewis, G. R., et al. 2007, GeoRL, 34, L22103
Crary, F. J., Magee, B. A., Mandt, K., et al. 2009, P&SS, 57, 1847
Cravens, T. E., Vann, J., Clark, J., et al. 2004, AdSpR, 33, 212
Cui, J., Yelle, R. V., Strobel, D. F., et al. 2012, JGR, 117, E11006
Edberg, N. J. T., Andrews, D. J., Bertucci, C., et al. 2015, JGR, 120, 8884
Edberg, N. J. T., Andrews, D. J., Shebanits, O., et al. 2013, JGR, 118, 5255
Erwin, D. A., & Kunc, J. A. 2005, PhRvA, 72, 052719
Erwin, D. A., & Kunc, J. A. 2008, JAP, 103, 064906
Galand, M., Yelle, R., Cui, J., et al. 2010, JGR, 115, A07312
Galand, M., Yelle, R. V., Coates, A. J., Backes, H., & Wahlund, J.-E. 2006, GeoRL, 33, L21101
Gronoff, G., Lilensten, J., & Modolo, R. 2009, A&A, 506, 965
Itikawa, Y. 2006, JPCRD, 35, 31
Koskinen, T. T., Yelle, R. V., Snowden, D. S., et al. 2011, Icar, 216, 507
Lavvas, P., Galand, M., Yelle, R. V., et al. 2011, Icar, 213, 233
Lavvas, P., Yelle, R. V., Koskinen, T., et al. 2013, PNAS, 110, 2729
Lean, J. L., Woods, T. N., Eparvier, F. G., et al. 2011, JGR, 116, A01102
Lewis, G. R., Arridge, C. S., Linder, D. R., et al. 2010, P&SS, 58, 427
Linder, D. R., Coates, A. J., Woodliffe, R. D., et al. 1998, in Measurement Techniques in Space Plasmas: Particles, AGU Geophys. Monogr. Ser., Vol. 102 ed. R. E. Pfaff, J. E. Borovsky, & D. T. Young (Washington, DC: AGU Geophysical Monograph), 257
Liu, X., & Shemansky, D. E. 2006, JGR, 111, A04303
Majeed, T., & Strickland, D. J. 1997, JPCRD, 26, 335
Mandt, K. E., Gell, D. A., Perry, M., et al. 2012, JGR, 117, E10006
Rees, M. H. 1989, Physics and Chemistry of the Upper Atmosphere (Cambridge: Cambridge Univ. Press)
Richard, M. S., Cravens, T. E., Wylie, C., et al. 2015a, JGR, 120, 1264
Richard, M. S., Cravens, T. E., Wylie, C., et al. 2015b, JGR, 120, 1281
Robertson, I. P., Cravens, T. E., Waite, J. H., Jr, et al. 2009, P&SS, 57, 1834
Rymer, A. M., Smith, H. T., Wellbrock, A., Coates, A. J., & Young, D. T. 2009, GeoRL, 36, L15109
Sagnières, L. B. M., Galand, M., Cui, J., et al. 2015, JGR, 120, 5899
Samson, J. A. R., Haddad, G. N., Masuoka, T., Pareek, P. N., & Kilcoyne, D. A. L. 1989, JCP, 90, 6925
Samson, J. A. R., Masuoka, T., Pareek, P. N., & Angel, G. C. 1987, JCP, 86, 6128
Shebanits, O., Wahlund, J. E., Mandt, K., et al. 2013, P&SS, 84, 153
Shemansky, D. E., & Liu, X. 2005, JGR, 110, A07307
Simon, S., van Treeck, S. C., Wennmacher, A., et al. 2013, JGR, 118, 1679
Simon, S., Wennmacher, A., Neubauer, F., et al. 2010, P&SS, 58, 1230
Snowden, D., Yelle, R. V., Galand, M., et al. 2013, Icar, 226, 186
Strobel, D. F. 2010, Icar, 208, 878
Teolis, B. D., Niemann, H. B., Waite, J. H., et al. 2015, SSRv, 190, 47
Vigren, E., Galand, M., Yelle, R. V., et al. 2013, Icar, 223, 234
Vigren, E., Galand, M., Yelle, R. V., et al. 2015, Icar, 248, 539
Vuitton, V., Lavvas, P. L., Yelle, R. V., et al. 2009, P&SS, 57, 1558
Vuitton, V., Yelle, R. V., & McEwan, M. J. 2007, Icar, 191, 722
Wahlund, J.-E., Galand, M., Müller-Wodarg, I., et al. 2009, P&SS, 57, 1857
Waite, J. H., Jr., Young, D. T., Cravens, T. E., et al. 2007, Sci, 316, 870
Wellbrock, A., Coates, A. J., Jones, G. H., et al. 2013, GeoRL, 40, 4481
Wellbrock, A., Coates, A. J., Sillanpää, I., et al. 2012, JGR, 117, A03216
Westlake, J. H., Waite, J. H., Jr., Mandt, K. E., et al. 2012, JGR, 117, E01003
Woods, T. N., Eparvier, F. G., Bailey, S. M., et al. 2005, JGR, 110, A01312
Woods, T. N., Eparvier, F. G., Hock, R., et al. 2012, SoPh, 275, 115
Young, D. T., Berthelier, J.-J., Blanc, M., et al. 2004, SSRv, 114, 1